Enhanced Photoactivity and Conductivity in Transparent TiO_2 Nanocrystals/Graphene Hybrid Anode

C. Ingrosso,[a, ‡,*] G. V. Bianco,[b,‡] V. Pifferi,[c] P. Guffanti,[c] F. Petronella,[a] R. Comparelli,[a] A. Agostiano,[a,d], M. Striccoli,[a] I. Palchetti,[e] L. Falciola,[c] M. L. Curri[a] and G. Bruno[b]

An optically transparent and UV-light active anode, characterized by high (photo)conductivity, charge mobility and exciton lifetime, based on graphene, grown by CVD, decorated with colloidal TiO_2 nanocrystals (NCs), has been fabricated, by a direct and facile solution-based procedure. TiO_2 NCs anchor onto graphene by means of π-π stacking interactions occurring between the pyrene-1-butyrric acid (PBA) surface coating ligand and the 2-D platform and assemble in a highly interconnected multilayered layout, by means of interligand π-π forces, retaining composition and geometry, along with graphene structure. Remarkably, the PBA-coated TiO_2 NCs on the graphene increase electrical conductivity, electroactivity, capacitive behavior, as well as photoelectrical response under UV-light, resulting in a 50% enhanced photoelectroactivity and a long exciton recombination lifetime. The photoanodes can be integrated in solar cells as optically transparent electrodes, in photodetectors and in FETs or (bio)sensors.

Introduction

Graphene, a 2-D polycrystalline and flexible material, based on a honeycomb sp_2-hybridized carbon atom structure, possesses unique structural properties, including optical transparency from visible to infrared, excellent thermal and electrical conductivity, high surface area, good biocompatibility, high flexibility and environmental stability.[1-3] Graphene based composites are increasingly investigated as effective structural materials to integrate in field-effect transistors (FETs), sensors, supercapacitors, touch panels, lithium-ion batteries, field emitters and solar cells.[4-7]

The high reactivity of the graphene platform offers diverse routes for the fabrication of hybrid composites by means of diverse nanostructured compounds, thus enabling the implementation of a great variety of decoration approaches. Such composites exhibit unique properties originated from the synergic combination of the single components, resulting in a material with novel functionalities not intrinsically exhibited by the bare graphene, such as light harvesting in the visible and infrared spectral range and selective molecular recognition abilities, improved electrical, mechanical and thermal properties and with enhanced (photoelectro)catalytic and photoelectrical conversion properties.[8]

Organic capped nanocrystals (NCs), prepared by means of solution-based colloidal chemistry routes, are functional nanomaterials exhibiting unique size- and shape-dependent properties, that are extremely suited for chemically decorating graphene, and for conveying therein the original NC functionalities, ultimately holding a great promise for advanced technological applications. The surface of the colloidal NCs, coordinated by surfactant molecules, can be chemically engineered by means of flexible post synthesis functionalization procedures, and thus enabling a proper tuning of the NC mutual and NC-substrate interactions. NC surface functionalization has demonstrated very effective in the fabrication of multilayered assemblies and hierarchical structures, as well as in the realization of hybrid composites, exhibiting multiple functionalities with a great potential in a variety of applications in (bio)sensing, photovoltaics and photocatalysis.[9]

In this work, a direct method has been used to functionalize graphene, grown by chemical vapor deposition (CVD), with pyrene-1-butyrric acid (PBA)-coated TiO_2 NCs. CVD grown graphene is a scalable material, suited for large-scale applications. CVD graphene finds applications into a variety of technologies, since it can be transferred onto several substrates (i.e. glass, silicon or polymer substrates) also in multilayers, showing different physical and chemical properties.[10]

On the other hand, TiO_2 is a wide band gap semiconductor and, in NC form, it is widely used in electrochemical sensors, solar cells and photocatalytic systems for its low toxicity, optical transparency in the visible range, low cost, biocompatibility, photostability and for its relevant photocatalytic and photoelectrochemical performance.[11-13]

The synergic combination of properties of the TiO_2 NCs and of the carbon based nanostructures has been demonstrated particularly suited to create hybrid materials with enhanced electrical conductivity, photoelectrical conversion efficiency, photocatalytic properties and environmental stability.[14] Indeed, in these composites, while the charge scavenger property of carbon based compounds decreases the recombination rate of photogenerated hole-electron pairs in TiO_2, the photoexcited charge, transferred to the carbon nanostructure, improves its charge transport properties.[15]

The interphase between graphene and TiO_2 NCs is expected to play an essential role in determining the electron coupling of the components. Here, pre-synthesized TiO_2 NCs, natively coated with oleic acid, have been surface functionalized with PBA. The hybrid material has been fabricated by exposing the graphene film to a dispersion of the PBA surface coated TiO_2 NCs. Such a ligand, effectively coordinating the NC surface by means of the carboxylic group, is able to electrically interconnect the NCs and chemically bind them to graphene, by means of π-π stacking interactions. Moreover, pyrene acts as a channel at the interface for a hole transfer in the hybrid, which leads to a p-doping of graphene.[16]

The prepared hybrid material has been characterized by scanning microscopies, Raman spectroscopy, along with Hall and (photo)electrochemical measurements for investigating morphology, chemistry, structure, electrical and photoelectrical properties. The decoration of graphene with the PBA-coated TiO_2 NCs has effectively resulted in a hybrid material able to combine the electron acceptor and ballistic charge transport capability of graphene, with the UV-light harvester behavior of

the TiO_2 NCs. The hybrid is optically transparent and concomitantly exhibits enhanced electroactivity and photoelectrical conversion with respect to the bare graphene, overall resulting in long recombination lifetimes. Therefore, the great potential of such a material can be envisioned as UV-light photoactive component for optically transparent electrodes to integrate in solar cells, photodetectors, FETs and sensors.

Experimental section

Materials

All chemicals were used at the highest purity available and as received. Oleic acid (OLEA, 90%), titanium tetraisopropoxide ($Ti(OPri)_4$ or TTIP, 98.9%), trimethylamino-N-oxide dihydrate ($(CH_3)_3NO{\cdot}2H_2O$ or TMAO, 98%) were purchased from Fluka. 1-pyrene butyric acid (PBA), methanol and chloroform were purchased from Aldrich.

Synthesis of oleic acid (OLEA)-capped TiO_2 NCs.

Spherical in shape oleic acid (OLEA)-capped TiO_2 NCs were synthesized with a diameter of 6 nm under N_2 atmosphere using a standard air free technique,[17] starting from dried and degassed reactants. The synthesis of the NCs is performed at low temperature (80-100°C), by the hydrolysis of the TTIP precursor in OLEA surfactant, and in presence of ethylene glycol and of TMAO base which catalyses polycondensation reaction of the precursor. The as prepared OLEA-coated TiO_2 NCs were isolated from the reaction mixture by precipitation with methanol, and finally were dispersed in chloroform for obtaining optically transparent solutions.

Preparation of the 1-pyrene butyric acid (PBA)-coated TiO_2 NC modified graphene based hybrid material

Capping exchange of OLEA-capped TiO_2 NCs with 1-pyrene butyric acid (PBA). For the ligand exchange procedure, the as synthesized TiO_2 NCs were repeatedly washed with methanol to remove the excess of the OLEA ligand coordinating the NC surface. Chloroform solutions of PBA were added to the washed 5×10^{-2} M TiO_2 NC solution in 1:5 TiO_2/PBA molar ratio and the mixture was left to stir overnight at room temperature. The NCs were then washed with methanol to remove the aromatic ligand in excess and then dispersed in chloroform. Transparent solutions of PBA-capped TiO_2 NCs can be achieved (10^{-3} M), that are stable over months without further addition of PBA molecules.

Graphene growth by Chemical Vapour Deposition (CVD). Monolayer graphene with 50-110 μm^2 grain sizes was grown by CVD on 25 µm thick copper foils (Alfa Aesar, item No. 13382) in a typical quartz tube CVD reactor at 1000°C using CH_4/H_2 as precursors. The prepared graphene was then transferred onto 300 nm SiO_2/Si or ITO/glass substrates by using a thermal release tape and a water solution of ammonium persulfate (0.1 M) as copper etchant. Before graphene transfer, the SiO_2/Si substrates were treated with O_2 plasma for improving adhesion. Bilayer graphene samples were fabricated by transferring additional graphene layers onto the monolayer graphene. All graphene samples were dipped in toluene/ethanol/anisole (1/1/1) solution for removing any organic impurities of thermal tape traces.

Functionalization of CVD grown graphene with 1-pyrene butyric acid (PBA)-coated TiO_2 NCs. Large area monolayer graphene transferred on SiO_2/Si substrate or ITO was incubated in a 10^{-3} M chloroform solution of PBA-capped TiO_2 NCs for 48 h and finally rinsed with chloroform to remove NCs not specifically adsorbed.

Characterization and measurements

Spectroscopic characterization. Steady state UV–Vis absorption spectra were recorded with a Cary 5000 (Varian) UV/Vis/NIR spectrophotometer. All optical measurements were performed at room temperature. Mid-infrared spectra were acquired with a Varian 670-IR spectrometer equipped with a DTGS (deuterated tryglycine sulfate) detector. The spectral resolution used for all experiments was 4 cm^{-1}. For attenuated total reflection (ATR) measurements, the internal reflection element (IRE) used was a one-bounce 2 mm diameter diamond microprism. The solution or suspension of interest (3–5 µL) were cast directly onto the internal reflection element, on the upper face of the diamond crystal.

Raman spectra of graphene were collected using a LabRAM HR Horiba-Jobin Yvon spectrometer with a 532 nm excitation laser sources. Measurements were carried out under ambient conditions at a low laser power (1 mW) to avoid laser-induced damage. The Raman band recorded from a silicon wafer at 520 cm^{-1} was used to calibrate the spectrometer, and accuracy of the spectral measurement was estimated to be 1 cm^{-1}.

Transmittance spectra of CVD graphene as bare and modified by PBA and by PBA-coated TiO_2 NCs were recorded by means of an optical setup composed by a white light source, a light collecting system and an optical spectrometer (HR4000 from Ocean Optics).

Transmission Electron Microscopy (TEM). TEM analyses were performed by using a Jeol Jem-1011 microscope, operated at 100 kV. TEM images were acquired by a Quemesa Olympus CCD 11 Mp Camera. TEM images of organic-coated TiO_2 NCs were collected by dipping the 300 mesh amorphous carbon-coated Cu grid in chloroform solutions of TiO_2 NCs and leaving the solvent to evaporate. Size statistical analyses (NP average size and size distribution) of the samples were performed by freeware ImageJ analysis program. At least 150 NCs were counted for each sample.

Scanning Electron Microscopy (SEM). Field emission scanning electron microscopy (FE-SEM) was performed by a Zeiss Sigma microscope operating in the range 0-10 keV and equipped with an in-lens secondary electron detector and an INCA Energy Dispersive Spectroscopy (EDS) detector. Samples were mounted onto stainless-steel sample holders by double-sided carbon tape and grounded by silver paste.

Atomic Force Microscopy (AFM). Topography and phase mode AFM measurements were performed in air and at room temperature, by means of a PSIA XE-100 SPM system operating in tapping mode. A

silicon SPM sensor for noncontact AFM (Park Systems), having a spring constant of 42 N m^{-1} and a resonance frequency of 330 kHz, was used. Micrographs were collected on six distinct areas of samples, with a scan size area of 5 µm × 5 µm, by sampling the surface at a scan rate between 1.0–0.5 Hz and a resolution of 256 × 256 pixels. Topography AFM images were processed by using XEI software to obtain statistical data.

Electrical measurements. Electrical measurements were carried out using a four-probe contacts geometry in the Van der Pauw configuration on a sample area of 4x4 mm^2 by a fully automated Hall system (MMR Technologies, Inc.).

Electrochemical measurements. Electrochemical measurements were made in a three electrode cell, by using an Autolab PG-Stat 30 (EcoChemie B.V., The Netherlands) potentiostat/galvanostat, equipped by Nova 2.0 software for the result analysis. A platinum wire was used as a counter electrode, a saturated calomel electrode as a reference electrode and a modified ITO glass as a working electrode. The ITO glass supporting electrode was modified by transfer of CVD graphene, as monolayer and bi-layer, also functionalized with the PBA-coated TiO_2 NCs.

In each electrochemical experiment, 0.1 M $NaClO_4$ (Aldrich, ACS reagent, ≥ 98.0%) was used as supporting electrolyte, while 3 mM $[Ru(NH_3)_6]Cl_3$ and 3 mM $K_4[Fe(CN)_6]$ (Sigma-Aldrich) were chosen as electrochemical probes for electrode characterizations.

Cyclic Voltammetry (CV) was performed scanning the potential between -0.3 V and 1.2 V (SCE), with a 0.005 V step potential at different scan rates (from 0.01 V s^{-1} to 0.75 V s^{-1}). Electrochemical Impedance Spectroscopies (EIS) were made at four different potentials (-0.1 V, 0.1 V, 0.25 V and 1 V) in absence of chemical probes; frequencies between 65000 Hz and 0.1 Hz were explored and a sinusoidal potential curve with an amplitude of 10 mV was applied in all the cases. Impedance data were processed by Z-View 3.1 software.

Photocurrent measurements, performed according to the method already optimized in literature,[18-19] were made at 1 V, illuminating the working electrode at definite times with an UV Jelosil HG500 iron halogenide lamp, having a power density of 45 mW cm^{-2} and placed at a distance of 40 cm from the sample. All the measurements have been carried out in N_2 atmosphere after degassing the cell with nitrogen flow for at least 10 min. Results were normalized subtracting the lower photocurrent curve in order to compare the different photoelectrochemical responses.

The photocurrent transients were treated according to the method of literature[18-19] in order to extract the time values τ for charge recombination processes.

Results and discussion

Preparation and morphological investigation of the PBA-coated TiO_2 NC surface modified CVD graphene

Oleic acid (OLEA)-coated TiO_2 NCs have been synthesized by means of the colloidal chemistry route reported in [17] and, then, surface modified with pyrene-1-butyrric acid (PBA). The pyrene functionality has been selected as its chemistry is expected to connect the TiO_2 NCs to graphene via π-π interactions, and concomitantly to coordinate the NC surface by means of its end carboxyl moiety.[16]

Morphology, optical properties and surface chemistry of the organic-coated TiO_2 NCs have been investigated before and after the ligand exchange, in order to assess the effective NC surface chemistry modification and any possible change in their spectroscopic and structural properties.

Both the morphology and the spectroscopic characteristics of the NCs result preserved after surface treatment with PBA (see Panel A of Fig. S1 of Electronic Supplementary Information (ESI)). Indeed, the PBA-coated NCs retain their spherical shape, with a diameter of 6.0 ± 0.3 nm, maintain the featureless absorption in the UV and near visible spectral region, typical of the high band gap nanostructured semiconductor[17] and are stable in solution without any aggregation phenomena.

The infrared spectroscopy spectra (Fig. S1 in ESI, panel B) demonstrate the binding of pyrene molecules to the surface Ti^{4+} Lewis sites by means of the carboxylate anions in a chelating bidentate binding mode[20,21] (panel A of Fig. 1) and attest also for the presence of residual pristine OLEA ligand molecules coordinated at the surface of the TiO_2 NCs. Although a complete displacement of such a ligand has been found to occur upon multiple ligand exchange steps, such a procedure has resulted in a loss of stability of the NCs in solution, due to aggregation phenomena (data not shown), and therefore it has been not considered viable.

After decoration of the CVD graphene with the PBA-capped TiO_2 NCs, the surface morphology and chemical composition of the hybrid have been studied by Scanning Electron Microscopy, Energy Dispersive X-Ray Spectroscopy and Atomic Force Microscopy (see panels A-D of Fig. 1).

While the surface morphology of the bare CVD graphene appears flat (see SEM and AFM images in Fig. S2), the secondary electron microscopy image points out that the morphology of the hybrid is mainly characterized by the presence of nanostructures at the graphene surface (panel A in Fig. 1). Such structures are also evident in the AFM topography image reported in panel C, which shows an interconnected layout of grain-type structures up to 50 nm high. The consideration of the actual NC size, as estimated by TEM (panel A in Fig. S1), and of the dimension of the features imaged in panel C, clearly indicates a multilayered arrangement of the PBA-coated TiO_2 NCs.

The EDS analysis of the prepared samples on a silicon wafer, reported in the range between 0-6 keV (Panel B of Fig. 1), shows typical Kα line of O (0.525 keV) and Ti (4.512 keV) elements, supporting the effective functionalization of graphene with the PBA-capped TiO_2 NCs.

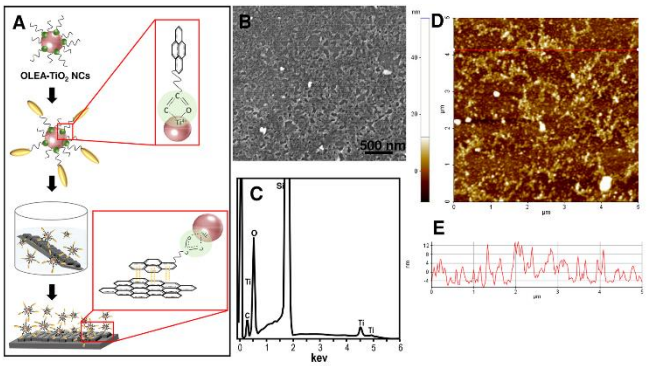

Fig. 1. (A) Scheme of functionalization of CVD grown graphene with PBA-coated TiO_2 NCs, with close-up views of the chemical interactions of PBA coordinated at the TiO_2 NC surface and of pyrene anchored on graphene. (B) SEM picture, (C) EDS spectrum in the range of 0-6 keV, (D) 2-D topography AFM image and (E) cross sectional line profile taken along the red line of panel D of CVD monolayer graphene functionalized with PBA-capped TiO_2 NCs.

The organization of the PBA-coated TiO_2 NCs in nanostructured assemblies, formed of tens nm high multilayers, can be reasonably ascribed to concomitant phenomena, namely i) multiple and cooperative π-π stacking interactions between the pyrene linker coordinating the TiO_2 NC surface and the graphene platform[16] (see Panel A in Fig. 1), ii) π-π interactions among the PBA molecules capping the NC surface and iii) interdigitation taking place between the alkyl chains of the residual OLEA ligand, with possible concomitant cross-linking of its -C=C- bonds.[22]

Spectroscopical and electrical investigation of the PBA-coated TiO_2 NC surface modified CVD graphene

Raman and Uv-VIS spectroscopy along with Hall measurements have been performed for investigating the structural and electrical properties of the CVD graphene films, decorated by the PBA-capped TiO_2 NCs. Fig. 2 reports the Raman spectra of the monolayer CVD-graphene transferred on SiO_2/Si substrate, before (black line) and after functionalization with the PBA-capped TiO_2 NCs (blue line).

The spectra of the bare graphene show the typical G and 2D peaks at 1583 cm^{-1} and 2678 cm^{-1}, respectively. In addition, the figure shows that at ca. 1350 cm^{-1}, the bare graphene does not exhibit the D peak, thus attesting for the very low density of C-sp^3 defects and, hence, for the high structural quality of the material. After decoration by the PBA-coated TiO_2 NCs, the D mode still shows a negligible contribution, as expected from the non-covalent nature of the graphene/PBA-capped TiO_2 NC chemical interaction. Conversely, the G and 2D peak positions, as well as the ratio between their intensities, drastically change after immobilization of the NCs. Namely, the stiffening of the Raman G and 2D modes from 1583 cm^{-1} to 1592 cm^{-1}, and from 2678 cm^{-1} to 2684 cm^{-1}, attests for the occurrence of charge transfer processes from graphene to the PBA-coated TiO_2 NCs.[16] Finally, three new peaks marked by the stars in panel A of Fig. 2 appear, which are accounted for by the typical Raman peaks of the pyrene rings.[23] The charge transfer from graphene to the PBA-coated TiO_2 NCs has been also assessed by Hall measurements.

The Hall measurement of the pristine CVD monolayer graphene shows a slight hole-doping that is typically accounted for by adsorption of air contaminants, such as H_2O and CO_2, acting as electron-withdrawing species.[24] We found a hole concentration, *n*, of 1.06 *10^{12} cm^{-2} which provides a shift of the graphene Fermi level (ΔE_F, referring to the Dirac point) of 0.12 eV, as derived by the following equation:[23]

$$\Delta E_F = h^* v_F (n/4\pi)1/2$$

where v_F is the Fermi velocity of 1.1 x 10^8 cm s^{-1}.

After decoration of graphene with PBA-coated TiO_2 NCs, the hole-doping further increases up to 2.13*10^{12} cm^{-2}, providing a ΔE_F of 0.17 eV and a decrease of the graphene sheet resistance from 1670 Ohm sq^{-1} to 834 Ohm sq^{-1}, without no substantial effects on the material charge carrier mobility (around 3500 $cm^2 V^{-1}s^{-1}$). Similar results have been previously reported by Liu et al.[25] for a TiO_2/graphene hybrid system, where the TiO_2 nanoparticle based film was directly deposited on graphene by radio frequency magnetron sputtering. Therefore, for the investigated hybrid system, the p-doping can be rationalized by a hole transfer from the nano-oxide to graphene,

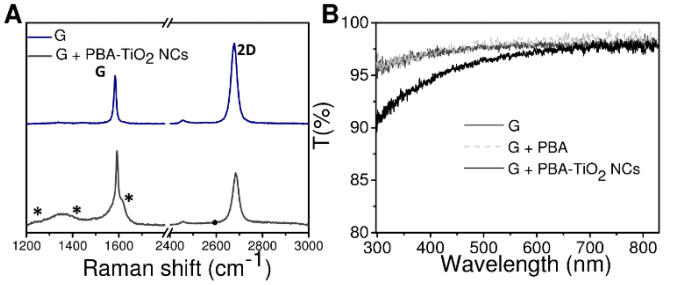

Fig. 2. Raman spectra of CVD graphene transferred on SiO_2/Si as bare and functionalized with PBA-capped TiO_2 NCs. (B). Transmittance spectra of CVD graphene as bare and modified by PBA and by PBA-coated TiO_2 NCs.

which is induced by the work function mismatch between graphene (≈4.50 eV) and the TiO_2 semiconductor (≈5.58 eV).

An essential role in such a hole transfer is played by the short chain aromatic pyrene linker[16] which acts as a channel of the charge coupling between the two materials. Indeed, in the PBA-capped TiO_2 NCs, holes are expected to be decoupled from the excited states and stabilized by the π ring system of pyrene by formation of a charge-separated complex, and then transferred to graphene or other TiO_2 NCs. The interligand interactions, occurring among adjacent NCs, can increase the charge mobility along the NC film, thus favouring the hole transfer also from the NCs not directly bound to graphene.

Optical transmission spectra have been collected for studying the spectroscopic properties of the hybrid material in the visible and near-UV spectral range. In particular, panel B of Fig. 2 compares the transmittance spectra of the bare graphene samples with those functionalized with PBA and with the PBA-coated TiO_2 NCs. The comparison of the spectra points out that the optical transparency of graphene in the visible range is not affected by the anchoring of the PBA ligand. After decoration with the NCs, it is only slightly reduced

by the immobilized TiO_2 NCs[17], namely it decreases down to 7.5% in the near UV spectral region.

Electrochemical properties of the PBA-coated TiO_2 NC functionalized CVD graphene

The electrochemical, electrical and structural properties at the PBA-coated TiO_2 NC/graphene junction of the hybrid material have been studied by Cyclic Voltammetry (CV) and Electrochemical Impedance Spectroscopy (EIS). For such a purpose, both mono and bilayer graphene films, have been decorated with PBA-coated TiO_2 NCs, by means of the same procedure described for the monolayer graphene films.

Indium Tin Oxide (ITO) electrodes have been modified by the prepared PBA-coated TiO_2 NC functionalized graphene. Namely, PBA-capped TiO_2 NC functionalized monolayer and bilayer graphene films (hereon indicated as $G1TiO_2$ NCs and $G2TiO_2$ NCs, respectively) have been manufactured, by transferring the CVD grown graphene on ITO, as described in the Experimental Section. Additionally, ITO electrodes, as bare and modified with both pristine monolayer (G1) and pristine bilayer graphene (G2), respectively have been tested.

The obtained working electrodes have been characterized by cyclic voltammetry (CV) at different scan rates, in a three-electrode cell by using 0.1 M $NaClO_4$ as a supporting electrolyte. With a potential window ranging between -0.3 V and 1.2 V (SCE), a 0.005 V step potential and a scan rate of 100 mV s^{-1}, the cyclic voltammograms (CVs) reported in panel A of Fig. 3, evidence that the anodic potential window limit of graphene, is affected by the immobilization of the TiO_2 NCs, anticipating the oxidation of the medium. Such a down-shift of the anodic potential (ca. 0.16 V) can be reasonably ascribed to the shift of the graphene Fermi level ΔE_F of ca. 0.17 eV, caused by the enrichment of holes transferred from the TiO_2 NCs, which makes the oxidation of the medium more energetically favourable. Panel A shows also that the down-shift of the anodic potential in the G1 and G2 graphene based electrodes is comparable.

Cyclic voltammetry profiles have been recorded in presence of an outer- and an inner-sphere probe, namely $[Ru(NH_3)_6]Cl_3$ and $K_4[Fe(CN)_6]$, respectively, in order to study the electron transfer and the structural quality of the prepared hybrid material based working electrodes. Panel B of Fig. 3 shows the CVs of modified electrodes recorded in the presence of the outer-sphere probe ($[Ru(NH_3)_6]Cl_3$). Such a molecule acts as an electron transfer redox probe exhibiting an electrochemical behaviour, which is affected by the electronic DOS of the electrode material.[26-28]

As it can be noticed from the figure, all the CVs of panel B present peak-shaped curves attesting for the fabrication of a continuous monolayer graphene film by CVD and for its effective and safely transfer on ITO glass supporting electrode. In addition, the CV line-shape is explained by a semi-infinite diffusion mechanism of the redox probe molecule towards the electrode (inset of panel B), which, hence, behaves as a "macroelectrode". [26-28] The different electrodes do not show peculiar differences, as only a very slight increase in the peak currents can be detected, probably due to an increase in the available electrode active surface.

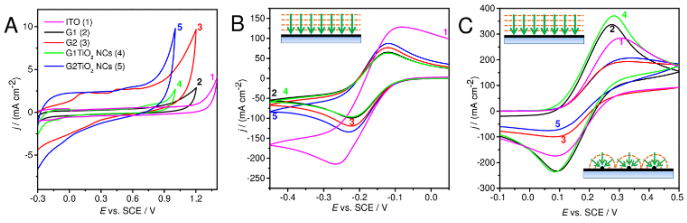

Fig. 3. CVs of bare (1) ITO glass, (2) monolayer graphene (G1), (3) bilayer graphene (G2) based reference electrodes and of (4) $G1TiO_2$ NC and (5) $G2TiO_2$ NC modified ITO glass electrodes. In A) background windows registered at 100 mV s^{-1} in 0.1 M $NaClO_4$. In B) peak-shaped CVs for the outer-sphere 3 mM $[Ru(NH_3)_6]Cl_3$ probe and (in the inset) sketch of the planar semi-infinite diffusion mechanism. In C) peak- and step-shaped CVs for the inner-sphere 3 mM $K_4[Fe(CN)_6]$ probe and (in the insets) sketches of planar semi-infinite (on the top) and convergent (on the bottom) diffusion mechanisms.

Finally, the more electrochemically reactive bilayer graphene film has been found sensitive to the decoration with the PBA-capped TiO_2 NCs. Indeed, an enhancement of the current density, after the NC decoration, has been observed, probably due to the increase of the active surface, because of the nanoporous structure, consistently with the results of the morphological investigation.

The modified electrodes have been voltammetrically characterized also in presence of the inner-sphere probe ($K_4[Fe(CN)_6]$), a molecule characterized by an electrochemical behaviour that is more sensitive to the chemistry (oxygen containing functionalities, impurities, adsorption sites) and structure of the electrode material surface, rather than its electronic density of states (DOS).[29,25-26] The corresponding CVs, reported in panel C of Fig. 3, show a different electrochemical behaviour for the mono and bilayer G films. In particular, the monolayer based electrodes show the peak-shaped curves, characteristics of the electrochemically inert side basal plane of a high quality and almost "perfect" monolayer graphene. As shown by the figure, such peak-shaped curves are characterized by a more reversible electrochemical behaviour (*i.e.* increased electron transfer rate) with respect to that of the bare ITO.[30] Conversely, the interaction of the inner-sphere redox probe with the bilayer graphene based electrodes leads to step-shaped voltammograms.[28] This result is explained by the sensitivity of the probe to the electro-active carbon-oxygen functionalities at the defects of the separated graphitic islands (grain boundaries, wrinkles, folded edges, peripheral edges, missing atoms, dandling bonds), which grow on the underlying continuous monolayer. Such islands are responsible for a convergent diffusion mechanism of the redox probe molecule to the electrode and result in the observed sigmoidal CVs typical of a "microelectrode".[26-27]

Upon immobilization of the PBA-coated TiO_2 NCs, neither the line-shape nor the current densities, reported in panel C, are affected, and this finding shows that the decoration procedure does not lead to structural defects on the graphene platform.

The electrical properties of the PBA-coated TiO_2 NC modified graphene hybrid material have been also studied by Electrochemical Impedance Spectroscopy (EIS) in 0.1 M $NaClO_4$ in a three electrode cell configuration.

Panel A of Fig. 4 reports the EIS Bode-phase plot of the working electrodes obtained in the dark at the potential of -0.1 V in the frequency range of 0.1-10000 Hz, while the corresponding Nyquist plots are reported in Fig. S2 of the Electronic Supplementary Information.

The G1 and G2 based working electrodes exhibit a different electrical behaviour, as a sigmoidal and peak-shaped EIS curves, respectively, have been recorded. Such curves have been fitted by using the Z-view software and the equivalent circuits reported in panels B and C of Fig. 4 have been achieved.

For the G1 electrode, the fitted equivalent circuit relays on the resistance R_Ω of the solution, in series with a capacitance C_1, which is ascribed to the "Debye layer", that is an accumulation of ions in proximity of the electrode, thus behaving as a parallel-plate capacitor, for compensating the charge accumulated at the graphene surface (panel B of Fig.4).

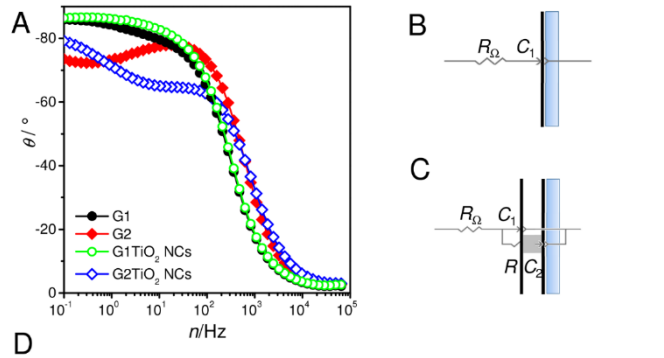

	C_1 / (μF cm^{-2})	α_1	R / (kΩ cm^2)	C_2 / (μF cm^{-2})	α_2
G mono	7.04 ± 0.04	0.92	-	-	-
G bi	3.80 ± 0.03	0.93	47 ± 3	2.71 ± 0.03	0.68
G mono + TiO_2 NCs	5.43 ± 0.02	0.95	-	-	-
G bi + TiO_2 NCs	6.77 ± 0.02	0.84	12 ± 1	3.62 ± 0.20	0.87

Fig. 4. EIS Bode-phase plots of G1, G2, G1TiO_2 NCs and G2TiO_2 NCs, respectively in the dark at the potential of -0.1 V in 0.1 M $NaClO_4$. (B-C) Equivalent circuits used for fitting the spectra of panel A. In B) G1 and in C) G2 based circuits. D) Values of the equivalent parameters of the circuits of panels B and C, estimated by fitting the EIS spectra.

Conversely, the equivalent circuit of the G2 based electrodes (panel C of Fig. 4) presents, in parallel with the interfacial capacitance C_1, a resistance *R*, which originates mostly from the turbostratic regions that are the graphitic islands of the second layer of graphene, which are not aligned with the underlying monolayer graphene basal plane. Such a misalignment leads to a contact resistance *R,* between the graphene layers, that can vary by more than one order of magnitude, depending on the angular alignment of the two graphene lattices.[31] In addition, in series with such a contact resistance *R*, the circuit in panel C presents also a capacitance C_2, originated from the charge separation between two graphene layers of the turbostratic regions.

The fitting procedure of the EIS Bode-phase plots reported in Fig. 4 allows estimating the values of the resistance and capacitance of the equivalent circuits, which are reported in panel D. Namely, the capacitance has been modelled as constant phase elements (CPE) by the following equation:

$$CPE = [(Ci\omega)^{\alpha}]^{-1}$$

where *C* is the capacitance, *i* the complex number, ω the frequency and α the parameter of deviation from the pure-capacitance behaviour, respectively.

The model provides for $\alpha = 1$, a perfect flat and continuous working electrode which behaves as a pure capacitor. On the other hand, if $0.5 < \alpha < 1$, a non-ideal capacitor behaviour is expected due to the non-homogenous porous electrode surface.

The values of the resistance and capacitance reported in panel D clearly show the different electrical proprieties of the manufactured working electrodes, evidencing the role of the immobilized PBA-coated TiO_2 NCs, on the parameters describing the equivalent circuits.

In case of the G1 electrodes, an interfacial capacitance (or electrical double layer capacitance) C_1, of ca. 7.04 μF cm^{-2}, has been estimated with a α_1 value very close to 1, namely 0.92, attesting for the high quality of capacitors based on monolayer graphene.

With the introduction of the second graphene layer, the electrodes still provide a capacitive behaviour, but the estimated value of C_1 is lower, namely ca. 3.80 μF cm^{-2}.

After immobilization of the PBA-coated TiO_2 NCs, the graphene electrodes present the same behaviour with smaller C_1 values with respect to monolayer graphene, and a slight increase passing from mono- to bi-layer (5.43 μF cm^{-2} and 6.77 μF cm^{-2}, respectively).

Such results are consistent with the recent report,[32] describing the capacitance as composed by two serial parts: the Helmholtz layer capacitance (C_H) and a quantum capacitance (C_Q), intrinsic to graphene. The two capacitive components act in different way: C_H decreases while C_Q raises with the increasing number of layers, resulting in a total capacitive behaviour presenting a maximum for intermediate layers. Moreover, C_Q is strongly influenced by the carrier density of graphene, *i.e.* by TiO_2 p-doping in our case. The resulting total capacitance depends on the balance of the variation of the previous described capacitances. According to these considerations, in our experiment, it seems that C_H variations prevail in the case of bare graphene, while for PBA-coated TiO_2 NCs the C_Q variations start to influence the total capacitive behaviour.

In case of the G2, the TiO_2 NC decoration also results in a decrease of the estimated resistance *R* between the two CVD graphene layers of the misaligned turbostratic regions, as well as an increase in the relative capacitance C_2. Such an evidence attests for an improvement of the graphene film structural quality, which can be related to the beneficial role of the pyrene capping ligand of the NCs in behaving as patches on the graphene discontinuities or defect regions,[33] as also confirmed by the α_2 value, which increases passing from 0.68 to 0.87.

Photoelectrochemistry of the PBA-coated TiO_2 NC functionalized CVD graphene

The photoelectrochemical properties of the PBA-coated TiO_2 NC surface modified CVD graphene have been studied by performing photocurrent measurements of the hybrid material under UV-light illumination. Panel A of Fig. 5 reports the photocurrent response of the manufactured working electrodes formed of bare and of PBA-coated TiO_2 NC functionalized graphene, under illumination with an UV-lamp (λ= 356 nm) at the bias voltage of 1V in 0.1 M $NaClO_4$. All the *I-t* curves appear anodic, thus accounting for the oxidation of the medium, with concomitant transfer of photogenerated electrons from the photoanode hybrid material to the ITO supporting electrode. In addition, the bare graphene based working electrodes show a photocurrent signal originated from the π-π* transition of the graphene -C=C- bond[34] that takes place under UV-irradiation. In particular, the G2 shows a photocurrent density higher than that of G1, namely 0.30 μA cm^{-2} against 0.15 μA cm^{-2} that can be explained by the linear increase of the broadband absorption of graphene, for increasing number of layers. Poor photocurrent density signals have been recorded for the PBA decorated G1 and G2 electrodes, namely about 0.11 μA cm^{-2} (see Fig. S4 of ESI). A negligible contribution to the photoresponse of graphene electrodes has been observed also

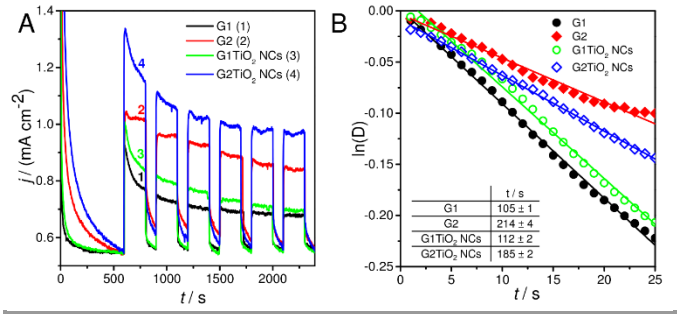

Fig. 5. (A) Photocurrent transient measurements collected under UV-light (λ=365 nm) irradiation at the bias voltage of 1 V in 0.1 M $NaClO_4$ and (B) normalized plot of current–time dependence of ITO electrodes modified with G1, G2 and PBA-coated TiO_2 NC functionalized G1 and G2 ($G1TiO_2$ NCs and $G2TiO_2$ NCs). (Inset of B) Transient time constants of the normalized plot of current–time dependence.

elsewhere for graphene electrodes modified by other pyrene compounds.[35]

On the contrary, the TiO_2 NC decorated graphene electrodes show an increase of the photocurrent density that has been found particularly evident in case of the $G2TiO_2$ NCs, whose value increases up to 0.45 μA cm^{-2}. These finding can be ascribed to the intrinsic UV-light activity of the TiO_2 NC film, which generates and keeps separated electron-hole pairs that can be then transferred to graphene, through the pyrene mediated electron coupling.

Indeed, pyrene linker stabilizes the photoelectrons by its π ring system and transfers them to graphene, where they can be stored in the extended π-π network of the aromatic platform. In addition, the Fermi level of graphene that lies in between the conduction band of TiO_2 and that of ITO, decreases the injection barrier at the ITO/TiO_2 NC interface. Finally, graphene, behaving as a charge acceptor and fast transporter, facilitates further photoelectron withdrawn from the TiO_2 NC film to ITO supporting electrode, suppressing both the hole/electron recombination processes at the defect states of the NC film and the back reactions at the interface with the electrolyte[36] finally resulting in an increase of the photocurrent.

The photoelectric properties of the prepared working electrodes and the charge recombination behaviour of the bare graphene and of the PBA-coated TiO_2 modified graphene electrodes have been further investigated, by studying the transient photocurrent decay that occurs immediately after UV-light illumination.

Panel B of Fig. 5 compares the logarithmic plots of the photocurrent transient decay D of the bare graphene based working electrodes with those of the PBA-coated TiO_2 NC modified homologues at the applied bias of 1 V. The transient decay time τ of the recombination of the photogenerated electron-hole pairs is defined as the slope of the ln(D) vs *t* curves[18] and it is reported in the inset of panel B.

Due to its high charge mobility, the pristine graphene based electrodes present extremely long electron recombination lifetimes τ, namely ca. 105 ± 1s for the monolayer and 214 ± 4 s for the bilayer, suggesting an efficient separation of the photogenerated carriers. After immobilization of the PBA-capped TiO_2 NCs on graphene, the electron recombination lifetimes of photogenerated electrons appear preserved, showing that the current leaking, due to recombination phenomena within the hybrid film and at the film/electrolyte interface, is limited and thus photoelectrons can be transported out quickly by graphene, improving anodic photocurrent. Thus, the hybrid shows an excellent merging of functionalities of both the components that are the highly conducting charge transport properties of graphene and the UV-light harvesting behaviour of the NC TiO_2, which result in an overall improved photoelectric conversion efficiency.

Conclusions

A straightforward and facile solution-based approach has been used to fabricate an optically transparent and UV-light active anode, integrating an hybrid material formed of a large area CVD grown monolayer graphene film, chemically decorated with a dense multilayered nanoporous coating of 1-pyrene butyric acid (PBA)-coated TiO_2 NCs.

The TiO_2 NC film acts as a p-doping and UV-light harvester layer, increasing graphene electrical conductivity, electrocatalytic activity and light-to-energy conversion. The assembling of the NCs, mediated by the stacking of pyrene, which acts as a beneficial patch of the graphene surface defects, preserves the excellent charge mobility and extremely long exciton lifetimes (ca. 185 ± 2 s) of graphene.

The manufactured photoanode has a relevant potential for integration in solar cells, photodetectors, catalytic systems, FETs and photoelectrochemical and capacitive sensors. Finally, the proposed strategy represents also an interesting model approach for the functionalization of graphene or other carbon based nanostructures with different types of nanoparticles, thus opening the venue to original classes of hybrid materials, relevant for a wide range of applications in different technological fields.

Acknowledgements

The authors acknowledge the National Project (PRIN 2012 prot. 20128ZZS2H) and the EU project TWINFUSYON (Horizon 2020, research and innovation programme under grant agreement No 692034).

Notes and references

1 K. S. Novoselov, A. K. Geim, S. V. Morozov, D. Jiang, M. I. Katsnelson, I. V. Grigorieva, S. V. Dubonos, A. A. Firsov, *Nature* 2005, **438**, 197.
2 C. Lee, X. Wei, J. W. Kysar, J. Hone, *Science* 2008, **321**, 385.
3 S. Stankovich, D. A. Dikin, G. H. B. Dommett, K. M. Kohlhass, E. J. Zimney, E. A. Stach, R. D. Piner, S. T. Nguyen, R. S. Ruoff, *Nature* 2006, **442**, 282.
4 E. Morales-Narváez, L. F. Sgobbi, L.F., S.A. S. Machado, A. Merkoçi, *Progress in Materials Science* 2017, **86**, 1
5 F. Schedin, A. K. Geim, S. V. Morozov, E. W. Hill, P. Blake, M. I. Katsnelson, K. S. Novoselov, *Nat. Mater.* 2007, **6**, 652.
6 J. T. Han, B. H. Jeong, S. H. Seo, K. C. Roh, S. Kim, S. Choi, J. S. Woo, H. Y. Kim, J. I. Jang, D.-C. Shin, S. Jeong, H. J. Jeong, S. Y. Jeong, G.-W. Lee, *Nat. Commun.* 2013**, 4**, 2491.
7 S. Bae, H. Kim, Y. Lee, X. Xu, J. Park, Y. Zheng, J. Balakrishnan, T. Kei, H. R. Kim, Y. I. Song, Y. J. Kim, K. S. Kim, B. Ozyilmaz, J. H. Ahn, B. H. Hong, S. Iijima, *Nat. Nanotechnol.* 2010, **5**, 574.
8 V. Georgakilas, J. N. Tiwari, K. C. Kemp, J. A. Perman, A. B. Bourlinos, K. S. Kim, R. Zboril, *Chem. Rev.* 2016*,* **116***,* 5464.
9 M. L. Curri, R. Comparelli, M. Striccoli, A. Agostiano, *Phys. Chem. Chem. Phys.* 2010, **12**, 11197.
10 Q. Yu, L. A. Jauregui, W. Wu, R. Colby, J. Tian, Z. Su, H. Cao, Z. Liu, D. Pandey, D. Wei, T. F. Chung, P. Peng, N. P. Guisinger, E. A. Stach, J. Bao, S. S. Pei, Y. P. Chen, *Nat. Mater.* 2011, **10**, 443.
11 V. Pifferi, G. Soliveri, G. Panzarasa, S. Ardizzone, G. Cappelletti, D. Meroni, L. Falciola, *RSC Advances* 2015, **5**, 71210.
12 G. Soliveri, V. Pifferi, G. Panzarasa, S. Ardizzone, G. Cappelletti, D. Meroni, K. Sparnacci, L. Falciola, *Analyst* 2015, **140**, 1486.
13 C. Chen, W. Cai, M. Long, B. Zhou, Y. Wu, D. Wu, Y. Feng, *ACS Nano* 2010, **4**, 6425.
14 H. J. Jeong, H. Y. Kim, H. Jeong, J. T. Han, S. Y. Jeong, K.-J. Baeg, M. S. Jeong, G.-W. Lee, *Small* 2014, **10**, 2057.
15 J. T. Han, B. J. Kim, B. G. Kim, J. S. Kim, B. H. Jeong, H. J. Jeong, S. Y. Jeong, J. H. Cho, G.-W. Lee, *ACS Nano* 2011, **5**, 8884.
16 C. Ingrosso, G. V. Bianco, M. Corricelli, R. Comparelli, D. Altamura, A. Agostiano, M. Striccoli, M. Losurdo, M. L. Curri, G. Bruno, *ACS Appl. Mater. & Interfaces* 2015, **7**, 15494.
17 P. D. Cozzoli, A. Kornowski, H. Weller, *J. Am. Chem. Soc.* 2003, **125**, 14539.
18 R. Dholam, N. Patel, A. Santini, A. Miotello, *Int. J. Hydrogen Energy* 2010, **35**, 9581.
19 F. Spadavecchia, G. Cappelletti, S. Ardizzone, M. Ceotto, M. S. Azzola, L. Lo Presti, G. Cerrato, L. Falciola, *J. Phys. Chem. C* 2012, **116**, 23083.
20 P. J. Thistlethwaite, M. S. Hook, *Langmuir* 2000, **16**, 4993.
21 M. Nara, H. Torii, M. Tasumi, *J. Phys. Chem.* 1996, **100**, 19 812
22 Odian, G. Principles of Polymerization, 4th ed.; Wiley: Hoboken, NJ, 2004; pp 737−738.
23 H. Shinohara, Y. Yamakita, K. Ohno, *J. Mol. Struct.* 1998, **442**, 221.
24 M. Lafkioti, B. Krauss, T. Lohmann, U. Zschieschang, H. Klauk, K. v. Klitzing, J. H. Smet, *Nano Lett.* 2010, **10**, 1149.
25 L. Liu, S. Ryu, M. R. Tomasik, E. Stolyarova, N. Jung, M. S. Hybertsen, M. L. Steigerwald, L. E. Brus, G. W. Flynn, *Nano Lett.* 2008, **8**, 1965.
26 X. Liu, R. Cong, L. Cao, S. Liu, H. Cui, *New J. Chem.* 2014, **38**, 2362
27 D.A.C. Brownson, D.K. Kampouris, C.E. Banks, *Chem. Soc. Rev.* 2012, **41**, 6944.
28 L. R. Cumba, C. W. Foster, D. A. C. Brownson, J. P. Smith, J. Iniesta, B. Thakur, D. R. do Carmo and C. E. Banks, *Analyst* 2016, **141**, 2791.
29 D.A.C. Brownson, C.E. Banks, *Phys. Chem. Chem. Phys*. 2011, **13**, 15825
30 A. Ambrosi, M. Pumera*, J. Phys. Chem. C* 2013, **117**, 2053.
31 S. Paulson, A. Helser, M. Buongiorno Nardelli, R. M. Taylor, M. Falvo, R. Superfine, S. Washburn, *Science* 2000, **290**, 1742.
32 H. Ji, X. Zhao, Z. Qiao, J. Jung, Y. Zhu, Y. Lu, L. L. Zhang, A. H. MacDonald, R. S. Ruoff, *Nat. Commun.* 2014, **5**, 3317
33 M. Zhang, R. R. Parajuli, D. Mastrogiovanni, B. Dai, P. Lo, W. Cheung, R. Brukh, P. L. Chiu, T. Zhou, Z. Liu, E. Garfunkel, H. He, *Small* 2010, **6**, 1100.
34 L. Li, X. Zheng, J. Wang, Q. Sun, Q. Xu, *ACS Sustainable Chem. Eng.* 2013, **1**, 144.
35 S. C. Feifel, K. R. Stieger, H. Lokstein, H. Luxc, F. Lisdata, *J. Mater. Chem. A* 2015, **3**, 12188.
36 N. Yang, J. Zhai, D. Wang, Y. Chen, L. Jiang, *ACS Nano* 2010, **4**, 887.

Graphical Abstract

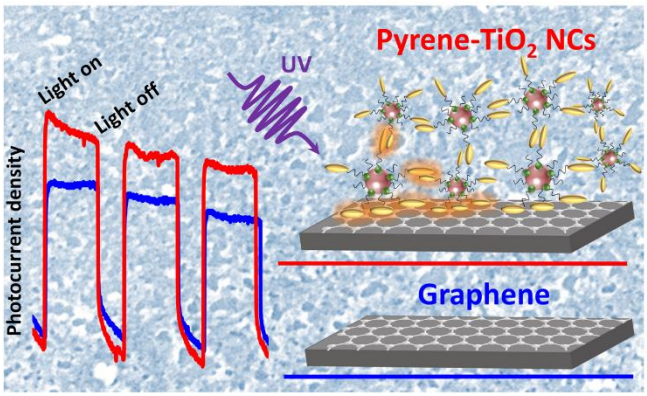

Electronic Supplementaty Information of Enhanced Photoactivity and Conductivity in Transparent TiO_2 Nanocrystals/Graphene Hybrid Anode

C. Ingrosso[a,‡,*] G. V. Bianco[b,‡] V. Pifferi,[c] P. Guffanti,[c] F. Petronella,[a] R. Comparelli,[a] A. Agostiano[a,d], M. Striccoli,[a] I. Palchetti,[e] L. Falciola,[c] M. L. Curri[a] and G. Bruno[b]

The inset of Panel A of Fig. S1 reports TEM images of as-synthesized OLEA-coated and PBA treated TiO_2 NCs. The as-synthesized nano-objects are spherical in shape and have an average diameter of 6 nm, appearing rather well spaced and separated on the grid, because of the presence of the long alkyl chain OLEA molecules,[1] and after the capping exchange with PBA the nanoparticles preserve their morphology. The same panel A of Figure 1 displays UV-Vis spectra of TiO_2 NCs, surface coordinated by OLEA and surface modified with PBA, respectively. Both spectra show the typical featureless line-shape of a high band gap TiO_2 semiconductor,[1] and upon treatment with PBA, the NCs almost display the same spectroscopic behavior.

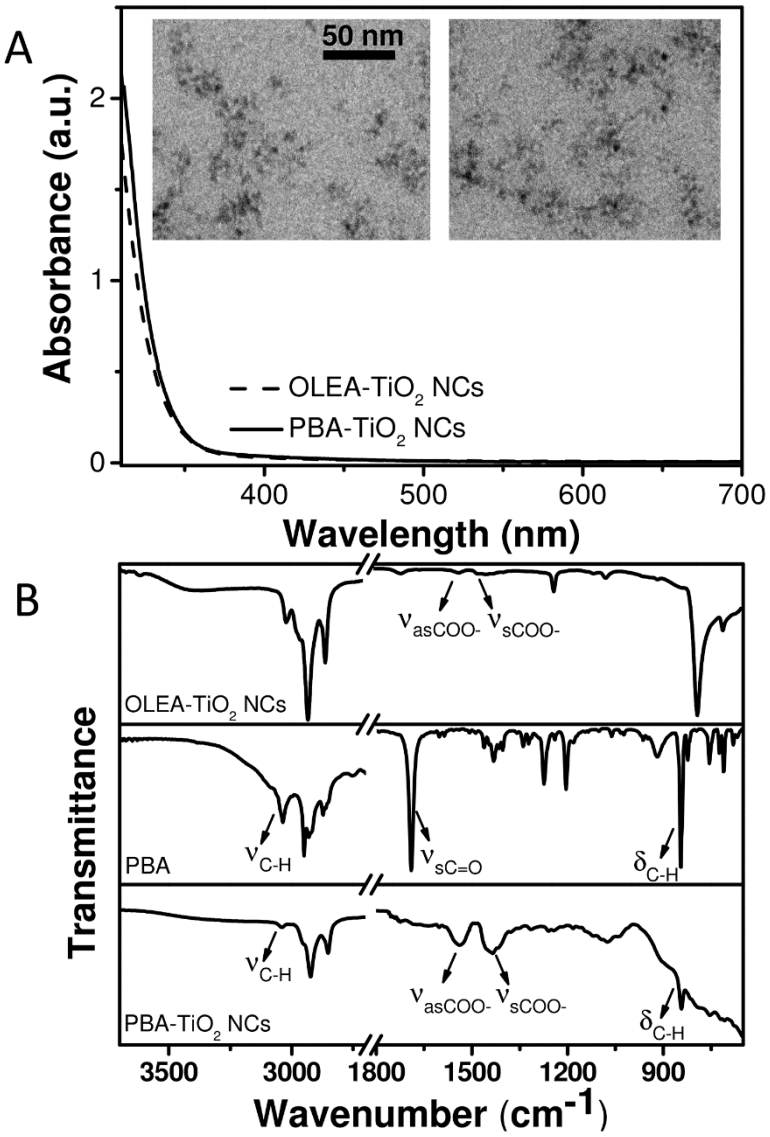

Fig. S1. (A) UV-vis absorption spectra and (in the inset) TEM micrographs of oleic acid (OLEA, left)- and pyrene butyric acid (PBA, right)-coated TiO_2 NCs. (B) ATR-FTIR spectra of OLEA-TiO_2 NCs, PBA and PBA-TiO_2 NCs.

Panel B of Fig.S1 compares the infrared spectra of the PBA-coated TiO_2 NCs with those recorded from the pristine OLEA-capped TiO_2 NCs and from bare PBA molecules. The high wavenumber region of the spectrum of PBA-capped TiO_2 NCs is characterized by the presence of typical signals of both PBA and residual OLEA ligand molecules. Namely, at 3039 cm^{-1} the aromatic C-H stretching vibration of pyrene molecule is evident, along with the strong band of the asymmetric -CH3 stretching at 2956 cm^{-1} and the strong asymmetric and symmetric

stretching of $–CH_2$- of OLEA at 2923 cm^{-1} and 2852 cm^{-1}, respectively. In the low wavenumber region of the spectrum of the PBA-coated TiO_2 NCs, the signals of the antisymmetric and symmetric -COO- stretching of PBA, namely $\upsilon_{as, CO2^-}$ at 1539 cm^{-1} and $\upsilon_{s, CO2^-}$ 1434 cm^{-1}, respectively which reasonably superimpose those of the residual OLEA molecules, expected at 1520 cm^{-1} and 1436 cm^{-1},[1] can be observed. The difference in Δυ of PBA, estimated as $\upsilon_{as, CO2^-} - \upsilon_{s, CO2^-}$, which is about 105 cm^{-1}, allows to infer the mode of binding as a chelating bidentate to the Ti^{4+} Lewis sites.[2,3] These findings, as well as the presence of the strong band pointed at 844 cm^{-1}, which is assigned to the characteristic out of plane C-H bending of the pyrene aromatic ring and the lack of the free C=O stretching band of the PBA and OLEA molecules, expected at 1691 cm^{-1} and around 1650-1720 cm^{-1}, respectively[1] allow to conclude that pyrene molecules coordinate the surface Ti^{4+} Lewis sites by the carboxylate anions in the form of a chelating bidentate binding. Fig. S2 reports the SEM and AFM images of the bare CVD graphene transferred on SiO_2/Si. The image shows an almost flat surface exhibiting striations in correspondence of grain boundaries and mechanical lattice deformations of the graphene plane[4] which bring to wrinkles or folds.

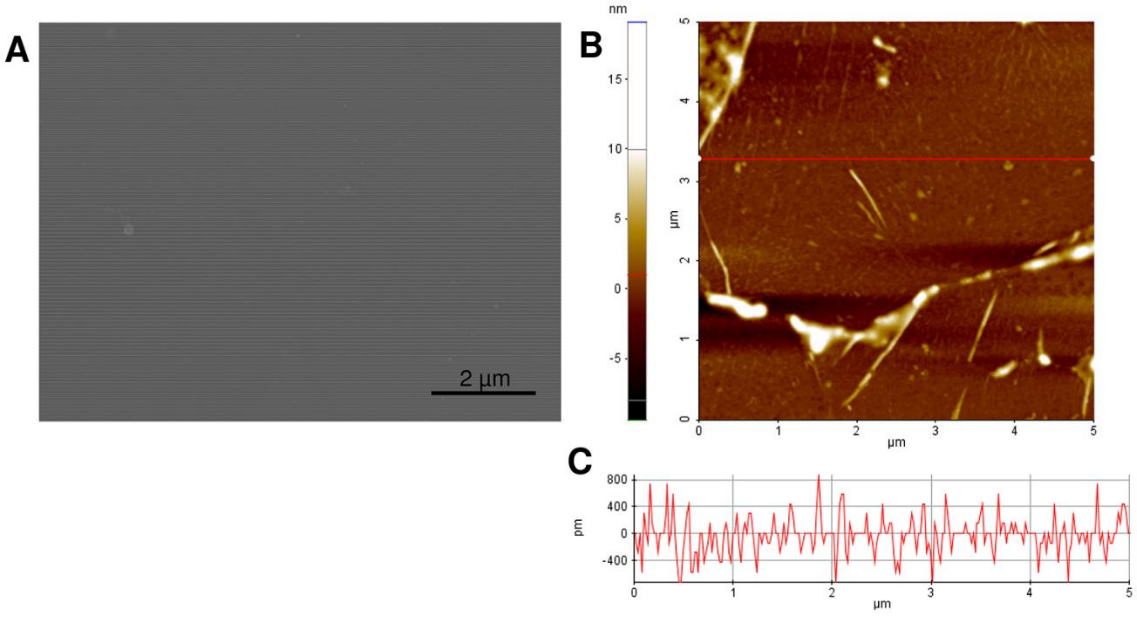

Fig. S2. (A) SEM and (B)2-D topography AFM images of CVD graphene transferred on SiO_2/Si substrate. In (C) cross sectional line profile recorded along the red line of (B).

Fig. S3 reports the EIS Nyquist plots of the ITO glass modified electrodes investigated in the work and registered in 0.1 M $NaClO_4$.

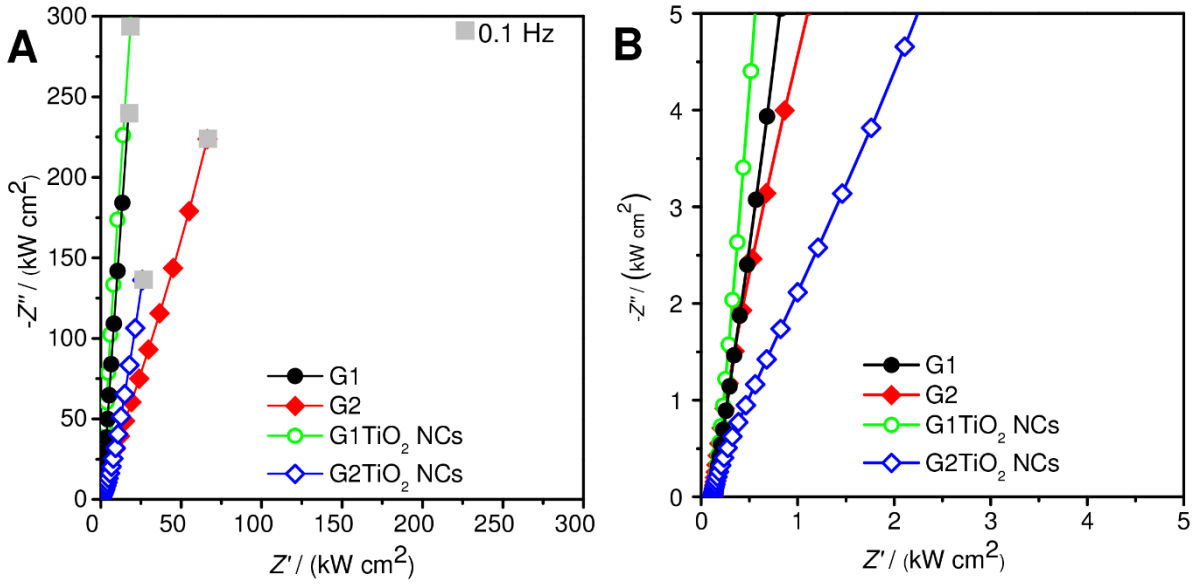

Fig. S3. EIS Nyquist plots of the ITO electrodes modified with monolayer graphene (G1), bilayer graphene (G2) and PBA-TiO_2 NCs functionalized monolayer and bilayer graphene ($G1TiO_2$ NCs and $G2TiO_2$ NCs) in 0.1 M $NaClO_4$.

Figure S4 reports the photocurrent response of the working electrodes formed of PBA surface coated mono (G1) and bilayer (G2) graphene, under illumination with an UV-lamp (λ= 356 nm) at the bias voltage of 1V in 0.1 M $NaClO_4$. The graphene electrodes have been functionalized by incubation for 48 h in a diluted solution of the PBA linker, namely 10^{-10} M. Such a value of concentration of the PBA linker has been selected because it is lower than the critical micelle concentration of pyrene, namely 10^{-7} M, at which pyrene compounds are expected to be in monomer form and not as micellar architectures of aggregates.[5]

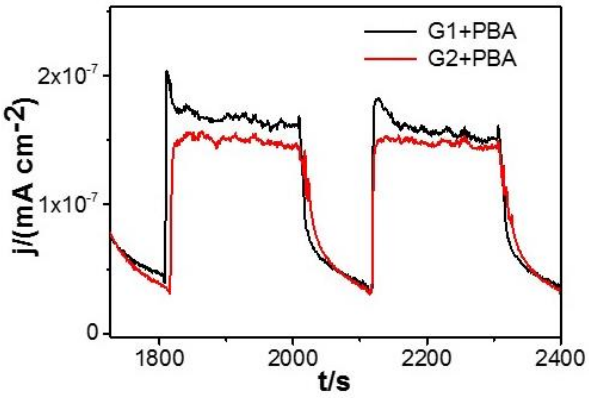

***Fig. S4**. Photocurrent transient measurements collected under UV-light (λ=365 nm) irradiation at the bias voltage of 1 V in 0.1 M $NaClO_4$ of ITO electrodes, modified with G1 and G2 surface coated by PBA.*

Fig. S4 shows that the photocurrent densities of the PBA coated G1 and G2 are about 0.11 µA cm^{-2}, hence lower than those of the corresponding samples functionalized with the PBA-coated TiO_2 NCs (panel A of Figure 5) and even lower than those of the bare G1 and G2, namely 0.15 µA cm^{-2} and 0.30 µA cm^{-2}, respectively, attesting for the poor effect that PBA has on the photoactivity of the CVD graphene film. Such results comply with the poor photocurrent density signals detected for the graphene electrodes modified by other pyrene compounds.[6]

References

1 P. D. Cozzoli, A. Kornowski, H. Weller, *J. Am. Chem. Soc.* 2003, **125**, 14539.

2 P. J. Thistlethwaite, M. S Hook, *Langmuir* 2000, **16**, 4993.

3 M. Nara, H. Torii, M. Tasumi, *J. Phys. Chem.* 1996, **100**, 19812.

4 M. Ahmad, H. An, Y. S. Kim, Y. S., J. H. Lee, J. Jung, S.-H. Chun, Y. Seo, *Nanotechnol.* 2012, **23**, 285705

5 M. Zhang, R. R. Parajuli, D. Mastrogiovanni, B. Dai, P. Lo, W. Cheung, R. Brukh, P. L. Chiu, T. Zhou, Z. Liu, E. Garfunkel, H. He, *Small* 2010, **6**, 1100

6 S. C. Feifel, K. R. Stieger, H. Lokstein, H. Luxc, F. Lisdata, *J. Mater. Chem. A* 2015, **3**, 12188.